RSC Advances

ROYAL SOCIETY OF CHEMISTRY

www.rsc.org/advances

Cite this: DOI: 10.1039/c0xx00000x

www.rsc.org/xxxxxx

Electrochemical energy storage and adsorptive dye removal of platanus fruit derived porous carbon

Xin Wang,[a] Zhiyong Gao,*[a] Jiuli Chang,[a] Dapeng Wu,[a,b] Xiaorui Wang,[a] Fang Xu,[a,b] Yuming Guo,[a,b] Kai Jiang*[a,b]

Received (in XXX, XXX) Xth XXXXXXXXX 20XX, Accepted Xth XXXXXXXXX 20XX
DOI: 10.1039/b000000x

Activated platanus fruit carbon (a-PFC) was synthesize by pyrolysis carbonization and alkali activation treatment of a easily available biomass, platanus fruit (PF). The carbonization yields platanus fruit carbon (PFC) sample with partially graphitized phase, and the followed KOH activation creates highly porous texture containing a large fraction of micropores and therefore a high specific surface area. Both of which are beneficial for surface relevant applications such as electrode material for electrochemical capacitor and adsorbent for sucking of organic dyes. The supercapacitor based on a-PFC$_3$, which was synthesized with KOH-to-PFC activation ratio of 3, offers a high gravimetric capacitance of 216 F g^{-1} at 1 A g^{-1}, a high rate performance and cycling stability, highlighting the potential of a-PFC$_3$ in electrochemical energy storage. The high specific surface area also makes a-PFC$_3$ an efficient adsorbent for sucking of methylene blue (MB) from aqueous solution.

Introduction

Energy and environment are two major topics that have attracted widespread concerns in scientific community. With the ever-growing consumption of fossil energy and the concomitant environmental pressure, it is necessary to develop reliable and sustainable energy sources without pollution emission. Supercapacitor is an attractive electrochemical power source owning superior power density, cycling stability, charging-discharging duration and operational safety over other rechargeable batteries, as well as the promptly increased capacitance and energy output,[1-3] hence it is regarded as a promising energy storage and supply device for portable electric products, electric vehicles, etc. Electrode material is the key component of supercapacitor, an ideal electrode material requires highly accessible surface area to electrolyte, well conductivity, structural stability and chemical inertness against electrolyte. On the other hand, organic dyes are important aquatic pollutions discharged from printing, dyeing, textile and painting industries, which seriously destroy the aquatic environment and may cause some threats to health. Because some dyes are difficult to be degraded, the adsorptive treatment is a feasible pathway to remove and even recycle them. The adsorptive treatment of organics necessitates highly porous adsorbent with high surface area and structural stability. Porous carbon can well meet the requirements of the abovementioned capacitive material and adsorbent. As a result, great efforts were devoted to the preparation of porous carbon materials and the applications in supercapacitor and organic dyes removal.

So far, various porous carbon materials including carbon nanotubes,[4,5] graphene[6,7] and hetero-elementals doped carbon[8-10] were synthesized as electrode materials for supercapacitors and demonstrated satisfactory performances. Meanwhile, these types of materials also showed high adsorption performances for removal of various dyes.[11-13] Albeit excellent performances were achieved from the abovementioned materials, the relatively high costs and somewhat tedious synthesis processes limit their widespread applications. More facile and cost-effective synthesis of porous carbon materials in bulk will promote the more extensive applications. Direct pyrolysis and activation of carbonaceous substances is a competitive approach to produce porous carbons in large scale. Biomass, especially vegetations represent a big class of cheap, easily available and renewable carbonaceous substances widely distributed on our planet that sustains the global water and carbon cycles. Due to the presence of rich capillaries for transportion of water and nourishments to sustain the growth, rich pores exist in vegetations, which make them ideal feedstocks for preparation of porous carbons with high surface areas. Pyrolysis is the most direct and facile approach to transform biomass into porous carbons. Due to the abundant resource with low costs, various natural biomass, including nut shell,[14,15] plant leaves,[16,17] fruit peels,[18,19] fish scales,[20] feathers,[21] hemp fiber[22] and wood sawdust[23,24] were widely employed as precursors for carbonization to generate porous carbon materials, and the afforded high capacitances or adsorption abilities highlighted the huge potential of biomass derived porous carbons in energy and environment related applications.

Platanus is a widely planted street tree for its strong adsorption ability toward dust and poisonous exhausts in urban atmosphere, excellent resistibility against contaminants, as well as the ultra-strong climate adaptability. The spheric fruit of platanus, namely PF contains numerous tiny fluffs, which is commonly undesirable and be discarded as waste owing to its allergy to certain susceptible population. Considering the possible high surface area associates with the slim and light fluffs, the carbonization can accomplish the resource utilization of PF and affords carbon materials for surface related applications, so the capacitive and adsorptive performances of PFC are expectable.

Herein, PF was employed as raw feedstock for the synthesis of porous carbon by pyrolysis and the subsequent alkali activation. The highly porous a-PFC demonstrated high BET surface area with overwhelming fraction of micropores, so the application performances in capacitive energy storage and adsorptive dye removal were tested and analyzed.

Experimental

Preparation of a-PFCs

All reagents in this work are of analytical grade and be used directly without further purification. Mature PF was collected after they fell from the platanus trees. The spheric PF was initially rinsed with deionized water to get rid of the adsorbed dust. After being dried and exfoliated, the inner fluff was used as crude material for carbonization and activation to afford a-PFC. In brief, the clean fluff was placed in a tube furnace and heated to 600 ^{o}C at a heating rate of 5 ^{o}C min^{-1} under N_2 atmosphere and then maintained at this temperature for 3 h. In the followed activation process, KOH was mixed with the obtained black PFC with mass ratio of 2, 3 or 4. Then the mixture was heated at 800 ^{o}C under N_2 atmosphere for 1 h for activation treatment. After being cooled naturally, the afforded a-PFC was washed copiously with diluted HCl and deionized water to eliminate the alkali and inorganics. The afforded a-PFC sample was denoted as a-PFC$_n$ (n = 2, 3 or 4, according to the KOH-to-PFC mass ratio).

Characterizations

The morphologies and microstructures of the samples were characterized by scanning electron microscopy (SEM, JEOL JSM-6390), high resolution transmission electronic microscopy (HRTEM, JEOL JEM-2100), X-ray powder diffraction (XRD, Bruker D diffractometer with Cu Ka radiation), Fourier Transform Infrared Spectroscopy (FTIR, Bio-Rad FTS-40) and X-ray photoelectron spectroscopy (XPS, ThermalFisher ESCALab 250 X-ray photoelectron spectroscopy with Al Ka radiation). Nitrogen adsorption-desorption isotherms were measured on a Micromeritics Gemini 2380 surface area analyzer at 77 K. The specific surface area was calculated by multiple point Brunauer-Emmett-Teller (BET) method. The micropore size distribution was estimated according to Horvath-Kawazoe (HK) theory. All the samples were degassed at 200 ^{o}C for 3 h prior to measurement.

Electrochemical measurements

Cycling voltammetry (CV) measurements of the electrodes were performed on a 660D workstation within potential range of 0~1 V in 1 M H_2SO_4. The three-electrode test system includes a stainless steel mesh work electrode coated with paste containing 85 mw% active material, 10 mw% acetylene black and 5 mw% polytetrafluoroethylene binder, a platinum wire counter electrode and a AgCl/Ag reference electrode. Galvanostatic charging-discharging curves of the symmetric capacitors (on Land CT2001A cell test system, Wuhan China) were tested in double-electrode mode in 1 M H_2SO_4 electrolyte over the voltage range of -1~1 V. The weight of active materials on each electrode was in the range of 1.5~2 mg, and the precise weights were measured accurately for gravimetric capacitances calculation. Electrochemical impedance spectroscopy (EIS) measurements of the electrodes were also performed on the same CHI 660D electrochemical workstation in three-electrode test system in 1 M H_2SO_4 electrolyte, impedances were recorded over the frequency range of 10^5~0.01 Hz with an ac perturbation of 5 mV.

The specific capacitance (C_s, F g^{-1}), energy density (E, Wh kg^{-1}) and power density (P, W kg^{-1}) of the symmetric capacitors were calculated from galvanostatic charging-discharging measurements according to the following equations:

$$C_s = I\Delta t/(\Delta V\times m) \qquad \text{(Eq. 1)}$$

$$E = C_s(\Delta V-IR)^2/8 \qquad \text{(Eq. 2)}$$

$$P = E/\Delta t \qquad \text{(Eq. 3)}$$

Where I (A) represents the discharge current, ΔV (V) is the voltage change within the discharge duration Δt (s), IR is the voltage drop owing to inner resistance at the initial stage of discharge process, m (g) is the total mass of active material on each electrode.

Adsorption measurements

The adsorption capability of a-PFC$_3$ adsorbent was evaluated using MB as adsorbate. Briefly, 10 mg of a-PFC$_3$ was sonically dispersed in the MB aqueous solution (350 mL, 20 mg L^{-1}) in dark to form a uniform dispersion. After that, the mixture was stirred at 20 ^{o}C. At different intervals, 2 mL of dispersion was sampled and centrifuged to afford supernatant, which was diluted to double volume for monitoring the adsorption kinetics and capacity *via* absorbances. In the adsorption isotherms measurements, 10 mg of a-PFC$_3$ was dispersed in 250, 275, 300, 325, and 350 mL of MB solution, respectively for adsorption treatment at 20 ^{o}C, and the relationship between equilibrium adsorption amounts (Q_{eq}) *and* equilibrium concentrations (C_{eq}) remaining in solutions was used for isothermal model fitting after the adsorption systems reach to equilibrium.

Results and discussion

Morphologies and microstructures

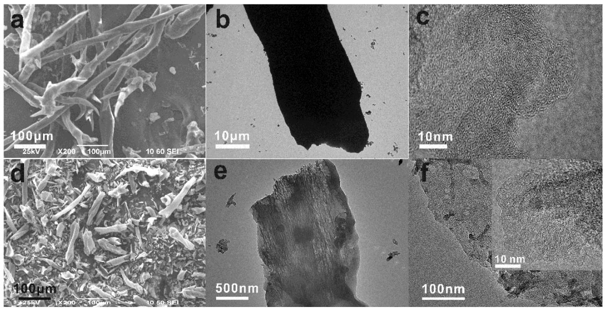

Fig. 1 (a, d) SEM and (b, c, e, f) TEM of (a-c) PFC and (d-f) a-PFC_3 at different magnifications.

Fig. 1 presents the morphologies and microstructure of PFC and a-PFC_3. PFC (Fig. 1a) exhibits tubular outline with outer diameter of up to 40 μm and length in millimeter scale, which resembles to the original appearance of raw PF fluff (not shown), implying the morphological dependence on the original PF source. KOH is a commonly employed porogen for carbon materials such as graphene, carbon nanotubes etc, due to the corrosive alkali can react with carbon framework to create rich pores and enhance the specific surface area.[7,22,25] The widely accepted mechanism of alkali activation follows the equation: $6KOH + 2C = 2K + 3H_2 + 2K_2CO_3$, and the produced potassium and its carbonate can further intercalate into graphitic carbon layers and etch the carbon skeleton to continue producing more open pores.[7,16,26] After being activated and etched by molten KOH at high temperature, the tubular PFC are damaged to different extents, as for a-PFC_3 activated with alkali-to-PFC ratio of 3, the long tubes are broken into segments with length shorter than 100 μm, the orifices at the tip clearly evidences the tubular shape. The short tube is beneficial for easier diffusion of electrolyte ions or organics into the inner surface with short channel length, hence the improved capacitive performance and adsorption capability are favorable.[27,28] TEM images (Fig. 1b and Fig. 1e) more clearly manifest the morphological change by alkali activation. PFC demonstrates 1-dimensional shape, the overall tube is dark, which is mainly due to the large diameter and the thick tube wall, electron beams can not penetrate the tube and results in the seemingly rod-like shape (Fig. 1b). After alkali activation (Fig. 1e), the enhanced transparency of the tube indicates the much hollowed interior of tube wall, which validates that KOH can etch PFC and create a substantial amount of micro/mesopores that are homogeneously distributed throughout the tube wall. More detailed observation reveals that the tube wall is composed of 1-dimensionally arranged mesopores (narrower than 50 nm) along the longitude direction, indicates that a-PFC_3 macrotube is actually composed of many primary nanotubes embedded in the tube wall. HRTEM image (Fig. 1c) of a PFC fragment shows alternative dark and light spots, revealing the presence of high density micropores in the tube wall, the sinuous fringes at the rim can also be easily observed, which is typical for carbon materials, indicating the graphitization of PFC. After alkali activation, the TEM still shows rich micropores (Fig. 1f). The wave shaped and incontinuous fringes (Inset) evidence that the high density of micropores destroy the continuity of graphitization regions throughout a-PFC_3. In this unique porous network with mesopores and micropores embedded into the tube wall of a-PFC_3, macropores and mesopores serve as main channel for electrolyte diffusion, the shorter length of a-PFC_3 by activation accelerate this process due to the short geometric distance, whereas the micropores provide major contribution to a high specific surface area, therefore electrolyte and organic molecules can readily infiltrate into the deep inner voids with huge interface area. Hence, a-PFC_3 is expected to be an efficient porous material in surface dependent applications e.g. electrode materials of capacitor and adsorbent for water treatment. Controlled samples with different KOH-to-PFC ratios are also characterized, a-PFC_2 shows longer macrotubes, while the length of a-PFC_4 is similar to a-PFC_3, meanwhile, more severe fragmentization occurs (Fig. S1), indicates the higher KOH dosage not only etches the carbon framework of PFC, but also causes the fracture and fragmentation of the carbon tubes. According to these results, the morphology, surface area, and therefore the application performances of a-PFC can be tuned by altering KOH activation dosage.

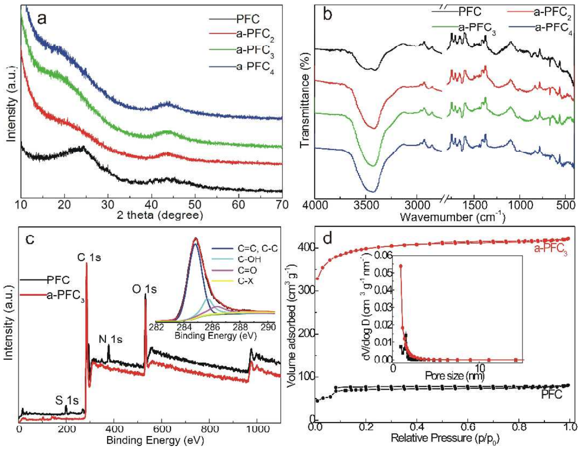

Fig. 2 a) XRD patterns, b) FTIR, c) XPS survey spectra, d) N_2 sorption isotherms and HK pore size distribution of PFC and a-PFC_3. Inset in panel c: C 1s spectrum of a-PFC_3.

Fig. 2a presents the XRD patterns of PFC and a-PFCs, two broad diffraction bands can be observed at 24° and 43° for PFC, which correspond to (002) and (110) facets of graphite-type carbon, the low intensity and broadness of the diffraction bands indicate the low crystallinity of PFC. After activation, the (002) diffraction band shift to lower angle, which is presumably due to the enlargement in interlayer distance of adjacent graphitized carbon layer by the introduced oxygen functional groups as spacer. In contrast, the intensity of (110) facet increases, which means higher integrity of in-plane graphitic carbon skeleton. From this phenomenon, the graphitization degree is actually increased by alkali activation at a higher temperature, although a high density of pores are created in carbon framework. As a whole, both of the diffraction peaks are still low, suggesting the largely amorphous nature the samples. Moreover, the high baseline in the low angle region for a-PFCs probably derives from the high density of micropores in carbon framework.[7]

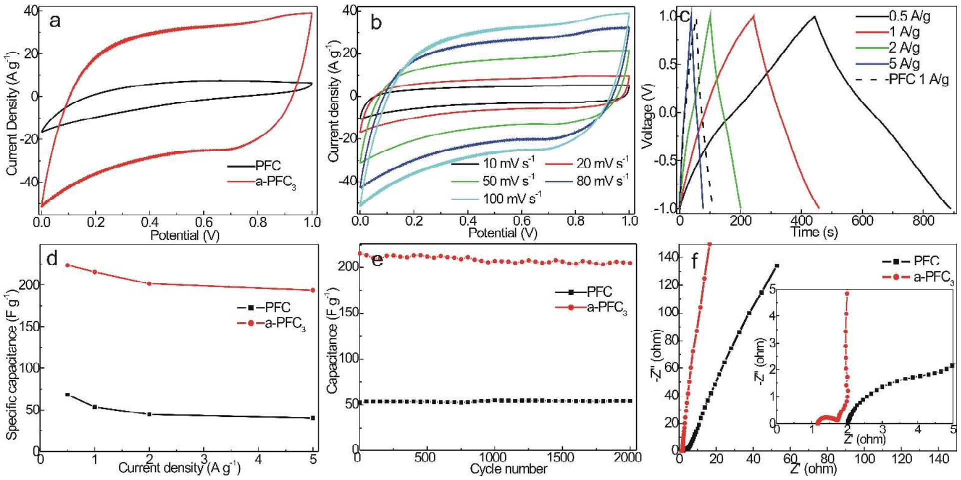

Fig. 3 a) CVs of PFC and a-PFC$_3$ electrodes at scan rate of 100 mV s^{-1} in 1 M H_2SO_4 electrolyte. b) CVs of a-PFC$_3$ electrode at different scan rates. c) Galvanostatic charge-discharge curves of symmetric capacitor in two-electrode mode based on a-PFC3 at different current densities, dashline: PFC capacitor at 1 A g^{-1}. d) Specific capacitances of PFC and a-PFC$_3$ based capacitors at different current densities. e) Cycling stabilities of PFC and a-PFC$_3$ based capacitors at 1 A g^{-1}. f) Nyquist plots of PFC and a-PFC$_3$ electrodes, inset: magnified impedance at high frequency region.

Fig. 2b shows the FTIR spectra of PFC and a-PFCs, the vibration peaks at 3420 cm^{-1} (stretching vibration mode) and 1635 cm^{-1} (bending vibration mode) indicate the presence of -OH groups in PFC and a-PFCs, the enhancement in intensity of both peaks for a-PFCs evidences that the activation treatment mainly produces plenty of hydroxyl groups in carbon framework. The vibration at 1726 cm^{-1} and 1680 cm^{-1} are attributed to -C=O in carboxyl and carbonyl motifs. All of these vibrations manifest the presence of hydroxyl, carbonyl and carboxyl in all the samples, thus offer essential hydrophilicity and polarity, allowing the accessibility of active surface to electrolyte ions and organics, which is also an indispensible factor for application as capacitive material and adsorbent for polar organics.

The surface chemical composition of PFC and a-PFC$_3$ are revealed by XPS analysis. From Fig. 2c, the survey spectrum of PFC (black curve) shows three peaks with binding energy at 284.8, 532.4 and 400.2 eV, which are characteristics of C 1s, O 1s and N 1s orbital, respectively, all these peaks indicate the surface composition of PFC comprises carbon, oxygen and nitrogen elementals. After alkali activation, the peak belonging to N 1s disappears in a-PFC$_3$ (red curve), suggesting the elimination of nitrogen elemental by activation treatment. Compared with PFC, the enhanced intensity of O 1s peak relative to C 1s in a-PFC$_3$ indicates the introduction of oxygen functional groups by alkali activation. The deconvoluted C 1s peak of a-PFC$_3$ shows the presence of C-C bond in graphite domains (284.8 eV), C-OH (285.7 eV) and C=O (286.5 eV) groups (inset), further verifies the partial graphitization of carbon framework and the presence of hydroxyl and carbonyl groups on a-PFC$_3$, which basically coincides with the XRD and FTIR data.

The pore properties of PFC and a-PFC$_3$ were analyzed by N_2 sorption isothermal measurements. As shown in Fig. 2d, both of the two samples demonstrate type I (Langmuir) isotherm coupled with a faint hysteresis loop characteristic of type IV isotherm according to IUPAC classification. Micropore filling occurs and quickly reaches to a saturated plateau at relative pressure lower than 0.15. The pronounced adsorption in this range evidences the presence of overwhelming micropores in both samples. These micropores are presumably derived from the intrinsic voids by evaporation of less stable substances inside PF during pyrolysis and activation treatment, which agree well with the TEM and XRD results. At relative pressure of 0.4-1, the low nitrogen adsorption amount and a weak but discernable hysteresis loop verify that only limited fraction of mesopores exists in both samples. The approximately H1 type hysteresis loop characterized by the parallel trend between adsorption and desorption branches indicates the slit-like geometry of mesopores, which associates with the embedded mesopores or capillary in tube wall of a-PFC$_3$ (Fig. 1e). The slight increment in adsorption amount at relative pressure approximate to 1 suggests the presence of a tiny fraction of macropores, which may be ascribed to the large internal diameter of PFC (or a-PFC) tubes. BET surface area and overall pore volume of a-PFC$_3$ are 1215 m^2 g^{-1} (1139 m^2 g^{-1} for micropores) and 0.65 cm^3 g^{-1} (0.58 m^2 g^{-1} for micropores) (Table S1). Both parameters are five times higher than the counterparts of PFC: BET surface area of 243 m^2 g^{-1} (216 m^2 g^{-1} for micropores) and pore volume of 0.12 cm^3 g^{-1} (0.09 cm^3 g^{-1} for micropores). Relative to PFC, micropores volumetric ratio of a-PFC$_3$ increases from 75 % to 88 %, manifesting the creation of more micropores by KOH activation, which may be due to the etching of carbon framework or the opening of dead pores in PFC by alkali activation. Moreover, HK pore size distribution calculated from adsorption branch shows enhanced probability below 2 nm, also verifies the increased micropores in a-PFC$_3$. No discernable pore size distribution over 2 nm can be observed, also confirms the much lower fraction of mesopores and macropores in a-PFC$_3$. The high BET surface area and versatile pore feature guarantee a highly accessible surface to electrolyte ions and organic molecules, facilitating the adsorption of more electrolyte ions and organics onto the entire surface of a-PFC$_3$, which will further result in a high electric-double-layer (EDL) capacitance and adsorption capacity for organics. KOH activation dosage dependent BET surface area and pore volume are also investigated (Fig.S2 and table S1), the specific surface areas of a-PFC$_2$ and a-PFC$_4$ are 954 and 1513 m^2 g^{-1}, respectively, indicates the higher alkali dosage is really beneficial for a high BET surface. Whereas the micropore volume ratio slightly decreases from a-PFC$_2$ to a-PFC$_4$, and the probability at larger pore size elevates simultaneously, both of these tendencies suggest that low dosage of KOH and the related corrosive species mainly intercalate into carbon layers and etch the carbon skeleton to create predominant micropores in a-PFC, if the KOH dosage is increased, the excessive corrosive species can further etch the rim of micropores and transform some of them into meso- or macropores. From these results, the specific surface area, pore volume and pore size can be roughly tuned by altering alkali dosage.

Electrochemical properties

The porous characteristics of a-PFCs with high surface area and partial graphitization make them good candidates as electrode materials for supercapacitor. To evaluate the capacitive performance of a-PFC, CVs of PFC and a-PFC$_3$ electrodes were measured at first in three-electrode system within potential range of 0~1 V at a scan rate of 100 mV s^{-1}. From Fig. 3a, both electrodes exhibit quasi-rectangular loop without obvious redox peaks, characteristic of typical EDL capacitive behavior. The dramatically higher plateau current and loop area of a-PFC$_3$ relative to PFC indicates the much higher capacitance of a-PFC$_3$, which is mainly attributed to the dramatic increment in BET surface area and therefore larger electrode/electrolyte interface area for ions accumulation. Additionally, the increased oxygen functional groups by activation enhance the wettability of a-PFC$_3$ to aqueous electrolyte, which also favors the readily infiltration and access to the deep inner voids, improving the surface utilization ratio of active material.

Fig. 3b presents the CVs of a-PFC$_3$ electrode at different scan rates. It is obvious that the plateau current increases accordingly with scan rate, and the quasi-rectangular loop can be largely retained without apparent distortion even at higher scan rate, evidencing the small inner resistance and fast electrolyte diffusion kinetics even at high scan rates, which further contributes to a high rate capability.

Fig.3c shows the galvanostatic charging-discharging curves of symmetric capacitors based on a-PFC$_3$ at various current densities in double-electrode mode. The approximately triangular charge-discharge branches with good symmetry and nearly linear discharging trend is indicative of typical EDL capacitance with rapid charging-discharging process. No discernable voltage drop can be observed at the beginning of the discharge stage even at current density of 5 A g^{-1}, validates the low intrinsic resistance of a-PFC$_3$, which may be attributed to the well conductivity of partially graphitized a-PFC after high temperature carbonization and activation treatment, as well as the rapid electrolyte diffusion kinetics owing to the versatile porous network with the coexistence of micro-, meso- and macropores. The discharging duration of a-PFC$_3$ at 1 A g^{-1} (red curve) is apparently longer than that of PFC (black dashline), implies the advantageous C_s of the former. From the discharging branch, C_ss of a-PFC$_3$ cell according to Eq. 1 are calculated to be 223, 216, 201 and 194 F g^{-1}, respectively at current density of 0.5, 1, 2, and 5 A g^{-1}, all of which are drastically higher than that of PFC based cell (Fig. 3d). It should be noted that the decrement in C_s at higher current density for a-PFC$_3$ is mainly caused by the insufficient diffusion of electrolyte into deep micropores at high current density. Albeit this, a 87 % C_s retention can still be achieved in the range of 0.5-5 A g^{-1} (Fig. 3d), revealing the high rate capability of a-PFC$_3$. We attribute to the high EDL capacitance and the rate capability to the unique electrolyte diffusion channel with the embedding of predominant micropores and small fraction of mesopores into the tube wall of a-PFC, which enables efficient infiltration and transfer of electrolyte ions into the deep inner void of porous electrode, maximizing the charge accumulation. Additionally, the partial graphitization of a-PFC benefits the rapid charge transfer during charging-discharging process. Both of these factors are essential for a high EDL capacitive performance.

Cycling performance of PFC and a-PFC$_3$ based capacitor were evaluated by consecutive galvanostatic charging-discharging measurements at 1 A g^{-1} (Fig. 3e). C_s of a-PFC$_3$ capacitor retains 91.2 % of its initial value after 2000 cycles, indicating a high degree of reversibility in the repetitive charging-discharging cycles. The high cycling performance can be attributed to the versatile pores and the well structural stability of a-PFC$_3$. The macropores and mesopores, although in limited fraction, benefit the shuttling of electrolytes, alleviating the over-accumulation of electrolyte in micropores and therefore the volumetric variation during charging-discharging cycles. Besides, the structural stability and chemical inertness of a-PFC$_3$ also help enduring the successive volumetric changes free of damage, both of which contribute to the high cycling stability. Although PFC possesses better cycling stability, the much lower C_s relative to a-PFC$_3$ limits its practical significance in capacitor applications.

To further understand the electrochemical behavior of a-PFC$_3$, EIS of PFC and a-PFC$_3$ electrodes were measured and compared, the Nyquist plots of both electrodes show similar shape, which comprise an unconspicuous semicircle in high-frequency region and a low-frequency straight line (Fig. 3f). The intercept at higher frequency end in real axis represents the series resistance (R_s), which includes the bulk electrolyte resistance, intrinsic active material resistance and the contact resistance between electrode and collector.[29,30] R_s values of PFC and a-PFC$_3$ are 2.0 and 1.2 Ω, respectively, the lower R_s of a-PFC$_3$ is presumably ascribed to the slightly higher graphitization degree relative to PFC (XRD in Fig. 2a) by activation at higher temperature, although the much hollowed texture is formed. The arc represents charge transfer resistance (R_{ct}) at electrode/electrolyte interface.[31,32] The lower R_{ct} for a-PFC$_3$ (0.5 Ω) than PFC (2.7 Ω) reflects a more rapid ions diffusion and accumulation on porous electrode surface, *viz* more efficient EDL capacitive behavior, which is due to the enhanced surface area and hydrophilicity after alkali activation. At lower frequencies, no distinct Warburg impedance can be observed for both samples (the line with slope angles near 45^{o}), which suggests the versatile pore network facilitates the rapid electrolyte diffusion kinetics. The more vertical straight line of a-PFC$_3$ at low frequency is indicative of a better EDL capacitive behavior with rapid ion diffusion kinetics. In short, by alkali activation at a higher temperature, lower R_s, R_{ct} and more efficient electrolyte diffusion kinetics can be achieved simultaneously in a-PFC$_3$, all of which eventually result in a substantial improvement in capacitive performance.

The effect of PFC-to-KOH activation ratio on the capacitive performance was also investigated (Fig. S3). As for a-PFC$_2$, due to longer tubes with lower BET surface area (Fig. S1 and Fig. S2), as well as the possibly smaller amount of hydrophilic oxygen functional groups owing to low alkali dosage during activation, a lower C_s of 202 A g^{-1} is obtained at 1 A g^{-1}. C_s of a-PFC$_4$ based capacitor (206 A g^{-1}) is elevated yet still lower than that of a-PFC$_3$ based cell, which is presumably due to the over hollowed texture by higher alkali activation dosage. The too high pore volume limits the conductive channel of porous electrode, which can be evidenced by the higher R_s whereas lower R_{ct} in impedance plots (green plots in Fig. S3d). In this sense, too high

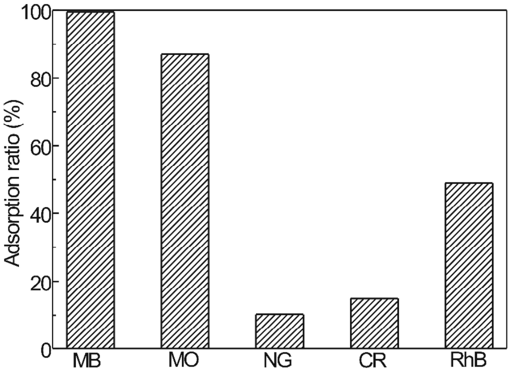

Fig. 4 Uptake ratios of different dyes by a-PFC$_3$.

or too low surface area is not necessarily beneficial for capacitance, an appropriate alkali dosage is essential to balance the contributions from conductivity and BET surface area. In a-PFC$_3$, the balanced factors result in a maximized capacitance. The rate performances of a-PFC$_2$ and a-PFC$_4$ are both slightly lower than a-PFC$_3$, further evidences the significance of alkali activation dosage on capacitive performance. Ragone plots shows that a-PFC$_3$ based capacitor offers a high energy density 30.4 Wh kg^{-1} at power density of 970 W kg^{-1} (Fig. S3e), both parameters are apparently higher than that of a-PFC$_2$ and a-PFC$_4$. The ultrahigh energy density herein is mainly attributed to the high C_s at low current density in aqueous electrolyte and the wide voltage window during discharging process. Hence, in our case, a-PFC$_3$ is a preferential electrode material with high capacitive performance.

Adsorption properties

Because of the high specific surface area and the porous feature with rich oxygen functional groups on the surface, a-PFC is thought to be an efficient adsorbent for organic dyes in aquatic environmental. Herein, the dye uptake capability of a-PFC$_3$ adsorbent was evaluated using MB, MO (methyl orange), NG (naphthol green), CR (congo red) and RhB (Rhodamine B) dyes as model adsorbates. The dye uptake capacity of a-PFC$_3$ can be easily estimated *via* monitoring the variation in absorbance. When 10 mg of a-PFC$_3$ was dispersed in 180 mL of different dye solutions (each is 20 mg L^{-1}), the adsorptive decoloration of dyes occured to different extents within 24 h (Fig. S4). As shown in Fig. 4, the uptake ratios of a-PFC$_3$ toward dyes differ apparently, almost 100 % of MB is removed from solution, which is higher than other dyes to different extents, revealing the well adsorption ability toward MB. The high MB adsorption ability may be attributed to the strong π-π stacking interaction between aromatic rings in MB molecules and the partially graphitized carbon skeleton of a-PFC$_3$, the anion-cation attraction between the positive charge of MB and the oxygen functional groups on a-PFC, hydrogen bonds, relatively lower steric hindrance of MB owing to the linear aligned aromatic rings, as well as the structural merits such as high BET surface area and versatile pore feature of a-PFC.

Due to the high uptake ratio for MB, the adsorption capacity for MB was evaluated. Q_{eq} (mg g^{-1}) for MB can be calculated based on the following mass conservation equation:[33]

$$Q_{eq} = (C_0 - C_{eq})V/m \qquad \text{(Eq. 4)}$$

Where C_0 and C_{eq} are the initial and equilibrium concentrations of MB (mg L^{-1}) in solution, V is the volume of MB solution (L), and m is the mass of adsorbent (g). Fig. 5a shows the plots of adsorption amount as a function of time in MB solution (20 mg L^{-1}, 350 mL), Q_{eq} for MB is estimated to be 550 mg g^{-1}. The value of Q_{eq} is higher over or comparable with the previous reported porous carbon materials,[11,34-37] revealing that a-PFC$_3$ is a competitive adsorbent for MB uptake. However, our value is still lower than that of other porous carbon or graphene due to the relatively lower surface area or the limited fraction of mesopores.[38-40]

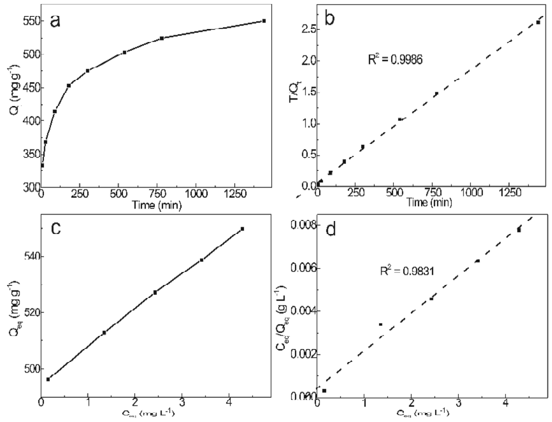

Fig. 5 a) Time dependent adsorption amount of MB on a-PFC$_3$. b) Pseudo-second-order adsorption kinetics. c) Adsorption isotherm of MB on a-PFC$_3$ at 20 °C. d) Plots of C_{eq}/Q_{eq} against Ceq based on Langmuir isotherm model.

The adsorption kinetics for MB was investigated by monitoring the decoloration rate relative to its initial absorbance. From Fig. 5a, it is clear that the adsorption rate is rather high in the initial 2 h and then gradually slows down and reaches a saturation platform within 24 h. The long adsorption duration herein is mainly due to the much higher volume of MB solution (350 mL) relative to a-PFC$_3$ dosage (10 mg), which restrains the diffusion and sufficient contact to a-PFC$_3$. The adsorption kinetic data was analyzed using a pseudo-second order kinetic model which based on the assumption that chemisorption is the rate determining step. The pseudo-second order kinetic model can be described as follows:

$$t/Q_t = 1/k_2\,Q_{eq}^2 + t/Q_{eq} \qquad \text{(Eq. 5)}$$

Where Q_t (mg g^{-1}) is the MB adsorption amounts at arbitrary time t, k_2 is the pseudo-second-order rate constant (g mg^{-1} min^{-1}). The plots of t/Q_t versus t are shown in Fig. 5b, the plots strictly obey the fitted straight line with a correlation coefficient of 0.9986, which is apparently higher than that fitted by pseudo-first-order kinetics equation (correlation coefficient: 0.9150, Fig. S5), verifies that the adsorption behavior follows more by pseudo-second-order kinetics, and k_2 is calculated to be 5.79×10^{-5} g mg^{-1} min^{-1}. According to this pseudo-second-order kinetics, the adsorption rate is dependent on both concentrations of absorbent and absorbate, a higher a-PFC$_3$ concentration in the dispersion should accelerate this chemisorption process and therefore shortens the adsorption duration.

Adsorption isotherm can be employed to elucidate the interactions between adsorbates and absorbent. Fig. 5c shows the adsorption isotherm of MB on a-PFC$_3$, Q_{eq} increased accordingly with C_{eq}. The experimental data was fitted by Langmuir isotherm, which assumes the homogeneous monolayer chemisorption of adsorbates on identical sites and the uniform adsorption energy due to the high affinity between adsorbate and adsorbent, the interactions between adsorbate molecules can be neglected. The Langmuir isotherm can be expressed as follows:

$$C_{eq}/Q_{eq} = C_{eq}/Q_{max} + 1/Q_{max} K_L \qquad \text{(Eq. 6)}$$

Where C_{eq} (mg L^{-1}) and Q_{eq} (mg g^{-1}) are the equilibrium concentration and adsorption capacity of MB, respectively, Q_{max} (mg g^{-1}) is the maximized MB adsorption amount, and K_L (L mg^{-1}) is the Langmuir adsorption constant. Fig. 5c displays the plots of Q_{eq} as a function of C_{eq} at different initial concentrations, Q_{eq} increases monotonously with C_{eq}. The plots of C_{eq}/Q_{eq} *vs* C_{eq} exhibits well linear relationship with correlation coefficient of 0.9831 (Fig. 5d), the value is higher than that fitted by Freundlich isotherm (correlation coefficient: 0.8699, Fig. S6), indicating the adsorption mode in our case follows more by Langmuir isotherm, of which the homogeneous monolayer chemical adsorption of MB occurs onto the possible homogeneous sites of a-PFC_3. Desorption of MB was attempted using acid, alkali or salts as elute, but failed, also suggests that the irreversible chemisorption by strong interactions between MB molecules and a-PFC_3.

Conclusions

In summary, a-PFC_3 was facilely synthesized by carbonization and alkali activation of PF. The as-prepared product demonstrated highly porous network with a large fraction of micropores, high BET surface area and partial graphitization, all of which lead to desired capacitive performances including high specific capacitance, rate capability and cycling stability when employed as electrode material for supercapacitor. Moreover, a-PFC_3 also showed high adsorption capacity for uptake of MB in aqueous solution. The well capacitive and adsorptive performances manifest the huge potential of a-PFC as energy and environmental materials.

Acknowledgements

This work was supported by NSFC (Nos. 61204078, U1304505, 61176004), Program for Innovative Research Team (in Science and Technology) in University of Henan Province (No. 13IRTSTHN026), Key Project of Science and Technology of Henan Province (No. 122102210561), Program for Changjiang Scholars and Innovative Research Team in University and the Key Project of Science and Technology of Xinxiang City.

Notes and references

[a] *School of Chemistry and Chemical Engineering, Henan Normal University, Henan Xinxiang 453007, P.R. China. E-mail address: zygao512@163.com (Z. Gao); Kjiang512@163.com (K. Jiang).*
[b] *Collaborative Innovation Center of Motive Power & Key Materials, Henan, 453007, P.R. China.*

1 H.B. Wu, H. Pang, X.W. Lou, *Energy Environ. Sci*., 2013, **6**, 3619.
2 C.L. Zhang, H.H. Yin, M. Han, Z.H. Dai, H. Pang, Y.L. Zheng, Y.Q. Lan, J.C. Bao, J.M. Zhu, *ACS Nano*, 2014, **8**, 3761.
3 Y.J. Zhang, Y.Y. Liu, J. Chen, Q.F. Guo, T. Wang, H. Pang, *Sci. Rep*., 2014, **4**, 5687.
4 M. Kaempgen, C.K. Chan, J. Ma, Y. Cui, G. Gruner, *Nano. Lett*., 2009, **5**, 1872.
5 P.X. Li, C.Y. Kong, Y.Y. Shang, E.Z. Shi, Y.T. Yu, W.Z. Qian, F. Wei, J.Q. Wei, K.L. Wang, H.W. Zhu, A.Y. Cao, D.H. Wu, *Nanoscale*, 2013, **5**, 8472.
6 X.W. Yang, C. Cheng, Y.F. Wang, L. Qiu, D. Li, *Science,* 2013, **341**, 534.
7 Y.W. Zhu, S. Murali, M.D. Stoller, K.J. Ganesh, W.W. Cai, P.J. Ferreira, A. Pirkle, R.M. Wallace, K.A. Cychosz, M. Thommes, D. Su, E.A. Stach, R.S. Ruoff, *Science,* 2011, **332**, 1537.
8 X.S. Du, C.F. Zhou, H.Y. Liu, Y.W. Mai, G.X. Wang, *J. Power Sources,* 2013, **241**, 460.
9 X.Y. Chen, C. Chen, Z.J. Zhang, D.H. Xie, X. Deng, J.W. Liu, *J. Power Sources*, 2013, **230**, 50.
10 M.X. Liu, L.H. Gan, W. Xiong, F.Q. Zhao, X.Z. Fan, D.Z. Zhu, Z.J. Xu, Z.X. Hao, L.W. Chen, *Energ. Fuel,* 2013, **27**, 1168.
11 Y. Chen, S.R. Zhai, N. Liu, Y. Song, Q.D. An, X.W. Song, *Bioresource Technol*., 2013, **144**, 401.
12 S.W. Zhang, M.Y. Zeng, J.X. Li, J. Li, J.Z. Xu, X.K. Wang, *J. Mater. Chem. A,* 2014, **2**, 4391.
13 S.B. Wang, H.Q. Sun, H.M. Ang, M.O. Tadé, *Chem. Eng. J*, 2013, **226,** 336.
14 A. Elmouwahidi, Z. Zapata-Benabithe, F. Arrasco-Marn, C. Moreno-Castilla, *Bioresource Technol.,* 2012, **111**, 185.
15 L. Sun, C.G. Tian, M.T. Li, X.Y. Meng, L. Wang, R.H. Wang, J. Yin, H.G. Fu, *J. Mater. Chem. A,* 2013, **1**, 6462.
16 R.T. Wang, P.Y. Wang, X.B. Yan, J.W. Lang, C. Peng, Q.J. Xue, *ACS Appl. Mater. Interf.,* 2012, **4**, 5800.
17 M. Biswal, A. Banerjee, M. Deo, S. Ogale, *Energy Environ. Sci*., 2013, **6**, 1249.
18 X. Li, W. Xing, S.P. Zhuo, J. Zhou, F. Li, S.Z. Qiao, G.Q. Lu, *Bioresource Technol*. 2011, **120**, 1118.
19 Y.K. Lv, L.H. Gan, M.X. Liu, W. Xiong, Z.J. Xu, D.Z. Zhu, D.S. Wright, *J. Power Sources,* 2012, **209**, 152.
20 W.X. Chen, H. Zhang, Y.Q. Huang, W.K. Wang, *J. Mater. Chem*., 2010, **20,** 4773.
21 Q. Wang, Q. Cao, X.Y. Wang, B. Jing, H. Kuang, L. Zhou, *J. Power Sources,* 2013, **225**, 101.
22 H.L. Wang, Z.W. Xu, A. Kohandehghan, Z. Li, K. Cui, X.H. Tan, T.J. Stephenson, C.K. King'ondu, C.M.B. Holt, B.C. Olsen, J.K. Tak, D. Harfield, A.O. Anyia, D. Mitlin, *ACS Nano,* 2013, **7**, 5131.
23 X.R. Liu, M.T. Zheng, Y. Xiao, Y.H. Yang, L.F. Yang, Y.L. Liu, B.F. Lei, H.W. Dong, H.R. Zhang, H.G. Fu, *ACS Appl. Mater. Interf.,* 2013, **5**, 4667.
24 E. Taer, M. Deraman, I.A. Talib, A. Awitdrus, S.A. Hashmi, A.A. Umar, *Int. J. Electrochem. Sc,*. 2011, **6**, 3301.
25 E. Raymundo-Pinero, P. Azaïsa, T. Cacciaguerraa, D. Cazorla-Amorósb, A. Linares-Solanob, F. Beguin, *Carbon,* 2005, **5**, 786.
26 M.A. Lillo-Rodenas, D. Cazorla-Amoros, A. Linares-Solano, *Carbon,* 2003, **41**, 267.
27 N. Liu, H.H. Song, X.H. Chen, *J. Mater. Chem*., 2011, **21**, 5345.
28 D.S. Yang, D. Bhattacharjya, S. Inamdar, J. Park, J.S. Yu, *J. Am. Chem. Soc.,* 2012, **134**, 16127.
29 L. Sun, C.G. Tian, Y. Fu, Y. Yang, J. Yin, L. Wang, H.G. Fu, *Chem. Eur. J.,* 2014, **20,** 564.
30 D. Puthusseri, V. Aravindan, S. Madhavi, S. Ogale, *Energy Environ. Sci.,* 2014, **7,** 728.
31 L.W. Su, Z. Zhou, M.M. Ren, *Chem. Commum*., 2010, **46**, 2590-2592.
32 L.W. Su, Y.R. Zhong, L.P. Wei, Z. Zhou, *RSC Adv*., 2013, **3**, 9035-9041.
33 L. Zhou, C. Gao, W.J. Xu, *ACS Appl. Mat. Interf.,* 2010, **5**, 1483.
34 L.H. Liu, Y. Lin, Y.Y. Liu, H. Zhu, Q. He, *J. Chem. Eng. Data,* 2013, **58**, 2248.
35 F. Liu, S. Chung, G. Oh, T.S. Seo, *ACS Appl. Mater. Interf.,* 2012, **4**, 922.
36 X.Y. He, K.B. Male, P.N. Nesterenko, D. Brabazon, B. Paull, J.H.T. Luong, *ACS Appl. Mater. Interf.,* 2013, **5**, 8796.
37 R.L. Liu, Y. Liu, X.Y. Zhou, Z.Q. Zhang, J. Zhang, F.Q. Dang, *Bioresource Technol*., 2014, **154**, 138.
38 B.B. Chang, D.X. Guan, Y.L. Tian, Z.C. Yang, X.P. Dong, *J. Hazard. Mater*., 2013, **262**, 256.
39 Y. Tao, D.B. Kong, C. Zhang, W. Lv, M.X. Wang, B.H. Li, Z.H. Huang, F.Y. Kang, Q.H. Yang, *Carbon,* 2014, **69**, 169.
40 T.T. Ma, P.R. Chang, P.W. Zheng, F. Zhao, X.F. Ma, *Chem. Eng. J.,* 2014, **240**, 595.